PAPER

Check for updates

Targeted synthesis and reaction mechanism discussion of Mo_2C based insertion-type electrodes for advanced pseudocapacitors†

Yuanyuan Zhu,‡[ae] Xu Ji,‡[b] Lufeng Yang,[c] Jin Jia,[d] Shuang Cheng, [iD] *[a] Hailong Chen,[c] Zhong-Shuai Wu, [iD] [e] Donata Passarello[f] and Meilin Liu [iD] [g]

Mo_2C is one of the few compounds that possess good electronic conductivity. Meanwhile, it possesses a natural 1D zigzag tunnel structure that is ideally suited for fast ion diffusion. Here, an effective approach is demonstrated for fabrication of structurally stable N-doped Mo_2C/C nanobelts. They demonstrate high and fast energy storage ability with initial capacitances of 1139 C g^{-1} at 1 mV s^{-1}, 151 C g^{-1} at an extremely high scan rate of 2000 mV s^{-1} and 208 C g^{-1} at a discharge current density of 200 A g^{-1}. After electrochemical activation of cycling, the capacity is continuously enhanced and much higher capacitances of 2523 C g^{-1} at 1 mV s^{-1} and 1403 C g^{-1} at 50 A g^{-1} are achieved after 15 000 cycles at 50 mV s^{-1}. Using the power law, it is evaluated that a surface-controlled capacitive process makes the main contribution to the capacity, which is over 90% when the scan rates are higher than 10 mV s^{-1} and still high as 73% at 1 mV s^{-1}. From *in situ* synchrotron XRD, it is found that there is a negligible change in the crystal structure and volume during charging/discharging, reflecting an insertion-type charge storage mechanism.

1. Introduction

Electrochemical capacitors with higher energy storage ability than conventional capacitors and better rate capacity and cycling life than batteries are becoming more and more attractive in many emerging fields,[1–3] such as electrical vehicles, portable electronics and smart grids for efficient and stable electrical energy storage. Electrical double-layer capacitors (EDLCs), as one of the two typical electrochemical capacitors,[4,5]

aNew Energy Research Institute, School of Environment and Energy, South China University of Technology, Guangzhou, 510006, People's Republic of China. E-mail: escheng@scut.edu.cn

bCollege of Automation, Zhongkai University of Agriculture and Engineering, Guangzhou, 510225, People's Republic of China

cThe Woodruff School of Mechanical Engineering, Georgia Institute of Technology, 771 Ferst Drive, Atlanta, GA 30332-0245, USA

dInstitute for Advanced Interdisciplinary Research, Collaborative Innovation Center of Technology and Equipment for Biological Diagnosis and Therapy in Universities of Shandong, University of Jinan, Jinan 250011, People's Republic of China

eDalian National Laboratory for Clean Energy, Dalian Institute of Chemical Physics, Chinese Academy of Sciences, 457 Zhongshan Road, Dalian 116023, People's Republic of China

fStanford Synchrotron Radiation Lightsource, SLAC National Accelerator Laboratory, Menlo Park, CA, USA

gSchool of Materials Science and Engineering, Georgia Institute of Technology, Atlanta, GA 30332-0245, USA

† Electronic supplementary information (ESI) available. See DOI: 10.1039/d0ta00697a

‡ Yuanyuan Zhu and Xu Ji contributed equally to this work.

store charge through the physical adsorption/desorption mechanism and hence exhibit a high rate capacity and durability but a low energy density.[6,7] Pseudocapacitors, in which much more charge can be stored *via* a faradaic reaction, are expected to store more energy than EDLCs.[8] Though various transition metal-based compounds have been explored as pseudocapacitive electrodes, they generally show unsatisfactory capacity, rate performance and cycling stability owing to their poor electronic/ionic conductivity and large volume change during cycling. To realize fast and high energy storage together with high durability, new potential candidates with an optimized structure and good electronic conductivity need to be developed.

Transition metal carbides (TMCs) are just one class of promising candidates, which usually originate from the introduction of carbon atoms into the metal lattice and exhibit novel and distinctive physical and chemical properties, including metallic conductivity and excellent corrosion resistance.[9–13] TMCs have been widely used in catalysis, electronics and other fields.[14–16] Since Gogotsi *et al.*[17] reported the electrochemical behavior of exfoliated Ti_2C as an anode for lithium-ion batteries in 2012, a series of carbides have been synthesized and used for lithium storage, such as Ti_3C_2,[18,19] Nb_2C,[20] V_2C,[21] Cr_2C[22] and Mo_2C.[23] Among them, Mo_2C, with a good electrical conductivity ($\sim 1.02 \times 10^2$ S cm^{-1})[24,25] and natural one-dimension (1D) tunnels that can serve as a fast ion diffusion path, is one of the most promising electrodes to balance capacity and rate performance. However, reports on

This journal is © The Royal Society of Chemistry 2020

J. Mater. Chem. A, 2020, **8**, 7819–7827 | **7819**

Mo_2C as an electrode are rare,[13,23] which is likely owing to its relatively low theoretical capacity, only 473 C g^{-1} (~131 mA h g^{-1}) when considering the transfer of one electron and 1892 C g^{-1} (~524 mA h g^{-1}) for the transfer of four electrons where full phase conversion of Mo_2C to Mo is predicted. Additionally, the synthesis of Mo_2C generally requires high-temperature calcination which would result in large bulks. Therefore, controlled-synthesis to realize the formation of nano-structured Mo_2C and the achievement of good charge storage performance are urgently needed.

Herein, a mild approach to prepare N-doped carbon coated Mo_2C (N-Mo_2C/C) nanobelts is proposed. Molybdenum source, MoO_3, pre-packaged with polypyrrole (PPY) is used as a precursor. N-Mo_2C/C delivers high initial capacitances of 1139 C g^{-1} at 1 mV s^{-1}, 151 C g^{-1} even at an extremely high scan rate of 2000 mV s^{-1} and 208 C g^{-1} at a discharge current density of 200 A g^{-1}, exhibiting high capacity and excellent rate performance. More importantly, there is no capacity fading but a continuous increase over the cycling test. After 15 000 cycles at 50 mV s^{-1}, significantly elevated capacitances of 2523 C g^{-1} at 1 mV s^{-1}, 2950 C g^{-1} at 0.5 A g^{-1} and 1403 C g^{-1} at 50 A g^{-1} are achieved. Using the power law, it is found that the energy storage is dominated by the surface-controlled capacitive process. Using *in situ* synchrotron XRD, the structural change during charging/discharging is explored. It is found that there is no phase change but slight expansion/contraction, implying an insertion-type charge storage process along the 1D tunnels.

2. Experimental

2.1 Materials and chemicals

Molybdenum powder (99.9%) is purchased from Aladdin Chemistry Co. Ltd (Shanghai, China). Hydrogen peroxide aqueous solution (H_2O_2, 30%) and ammonium persulfate are supplied by Damao chemical reagent factory (Tianjin, China). Pyrrole comes from Macklin Biochemical Co. Ltd (Shanghai, China). All the chemicals were used as received without further purification. Deionized water with a resistivity of 18.2 MΩ cm^{-1} is prepared using a Millipore purification system (Milli-Q®).

2.2 Preparation of the N-doped Mo_2C/C composites

Firstly, MoO_3 nanobelts are synthesized according to the following procedure: 1.0 g molybdenum (Mo) powder is added into 10 mL H_2O_2 (30%) solution and kept in an ice bath under stirring until a yellow solution is formed; then, 20 mL deionized water is added into the solution followed by continuous stirring for 30 min before being transferred into a 50 mL Teflon-lined stainless-steel autoclave for hydrothermal treatment at 200 °C for 24 h; after cooling to room temperature, a white precipitate of MoO_3 is collected through vacuum filtration, washed with deionized water and dried at 70 °C for 12 h. Secondly, MoO_3@ppy is obtained according to the following procedure: 0.1 g of the as-prepared MoO_3 is dispersed into 100 mL ammonium persulfate (7.5 mM) before 0.1 g pyrrole monomer is added for polymerization; the above solution is kept in an ice bath for 12 h under stirring; a black precipitate of MoO_3@ppy is

collected after vacuum filtration, washing and drying. Finally, the target sample of the N-Mo_2C/C powder is harvested through controlled calcinations at 700 °C for 4 h in flowing N_2.

2.3 Materials characterization

Phase compositions and crystal structure of the products were determined by X-ray diffraction (XRD) on a D8 Advance (Germany Bruker) X-ray diffractometer using Cu Kα radiation (λ = 0.15406 nm) at 40 kV and 40 mA. Morphologies of the products were observed using a field emission scanning electron microscope (FE-SEM, Hitachi SU8010) and a transmission electron microscope (TEM, JEM-2100F Field Emission Electron Microscope, Japan). X-ray photoelectron spectroscopy (XPS) was carried out on a PHI X-tool instrument (Ulvac-Phi). The Raman spectra were recorded using a LabRAM HR800 spectrometer (Horiba Jobin Yvon, France) equipped with a semiconductor laser (wavelength = 532 nm). The Brunauer–Emmet–Teller (BET) surface area was determined using a micromeritics ASAP 2020 analyzer with nitrogen adsorption at 77 K. Thermal Gravimetric Analysis (TGA) was performed using a Mettler-Toledo TGA/DSC1 apparatus between 30 °C and 700 °C at a ramping rate of 10 °C min^{-1} under an air flow.

Temperature-dependent *in situ* XRD patterns were collected using the same diffractometer mentioned above equipped with an Anton Paar XRK 900 high-temperature reaction chamber. The sample was heated from 30 °C to 700 °C with a heating rate of 5 °C min^{-1} under a N_2 flow with a space velocity of 30 mL min^{-1}. Before each XRD pattern was collected, the sample was held at a set temperature for 30 min. All the diffraction patterns were recorded in the range of 10–80° with a step size of 0.02° and a scanning rate of 0.08° s^{-1}.

In situ synchrotron X-ray diffraction (SXRD) was performed using a synchrotron radiation source (λ = 0.8856 Å) with beamline 7-2 in transmission mode, at Stanford Synchrotron Radiation Light source (SSRL), SLAC National Accelerator Laboratory Menlo Park, CA, USA. The patterns were collected every 2 min. The *in situ* test began with discharging from open circuit voltage and then charging in the range of 0.01–3 V (*vs.* Li/Li$^+$) at a current density of 0.2 A g^{-1} towards the half-cell with lithium foil as a counter electrode.

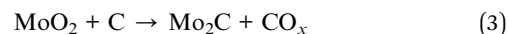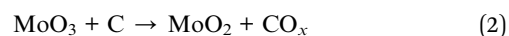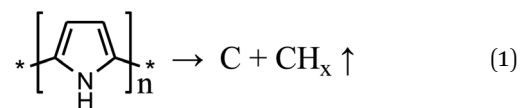### 2.4 Electrochemical measurements

Typically, working electrodes were prepared by mixing 80 wt% active materials, 10 wt% acetylene black, and 10 wt% poly-vinylidene difluorides in the *N*-methyl pyrrolidone (NMP) solvent. The slurry was coated on copper foil and dried before sealing in a CR2032 coin cell as an electrode using 1 M $LiClO_4$ in propylene carbonate, ethylene carbonate and dimethyl carbonate solution (a volume ratio of PC : EC : DMC of 1 : 1 : 1) with 5% fluoroethylene carbonate as an electrolyte and lithium wafer as a counter electrode, a typical half-cell. The assembly process was carried out in an argon-filled glove box with concentrations of moisture and oxygen below 0.1 ppm. The electrochemical performances were characterized by cyclic voltammetry (CV) and galvanostatic charge–discharge (GCD) techniques within a potential window of 0.01–3 V (*vs.* Li/Li$^+$)

7820 | *J. Mater. Chem. A*, 2020, **8**, 7819–7827

This journal is © The Royal Society of Chemistry 2020

using a CHI 660E electrochemical workstation. Electrochemical impedance spectra (EIS) were measured using a Solartron 1260 Impedance Analyzer in a frequency range of 0.1 Hz to 100 KHz with a perturbation voltage of 10 mV at open-circuit potential.

3.   Results and discussion

To take control of the phase change during calcination and optimize the target crystal structure, *in situ* XRD measurements were applied to the MoO$_3$@ppy precursor and a series of XRD patterns were collected upon increasing the temperature from 30 to 700 °C in N$_2$ flow, as presented in Fig. 1f. There is no phase change when the temperature is lower than 200 °C; while, PPY begins to be carbonized accompanied by the pulverization of MoO$_3$ at 300 °C; then MoO$_3$ is completely reduced to MoO$_2$ when the temperature is up to 400 °C; the MoO$_2$ phase is maintained in a relatively wide temperature range before it is

carbonized to be Mo$_2$C at 700 °C. Phase transition of MoO$_3$@-ppy can be expressed accordingly:[24]

$$\left[\underset{\underset{H}{N}}{\overset{}{\ce{}}} \right]_n \rightarrow C + CH_x \uparrow \tag{1}$$

$$MoO_3 + C \rightarrow MoO_2 + CO_x \tag{2}$$

$$MoO_2 + C \rightarrow Mo_2C + CO_x \tag{3}$$

The morphology change of the sample at different stages is characterized by SEM. The firstly synthesized MoO$_3$ is composed of nanobelts in a large-area with a width of around
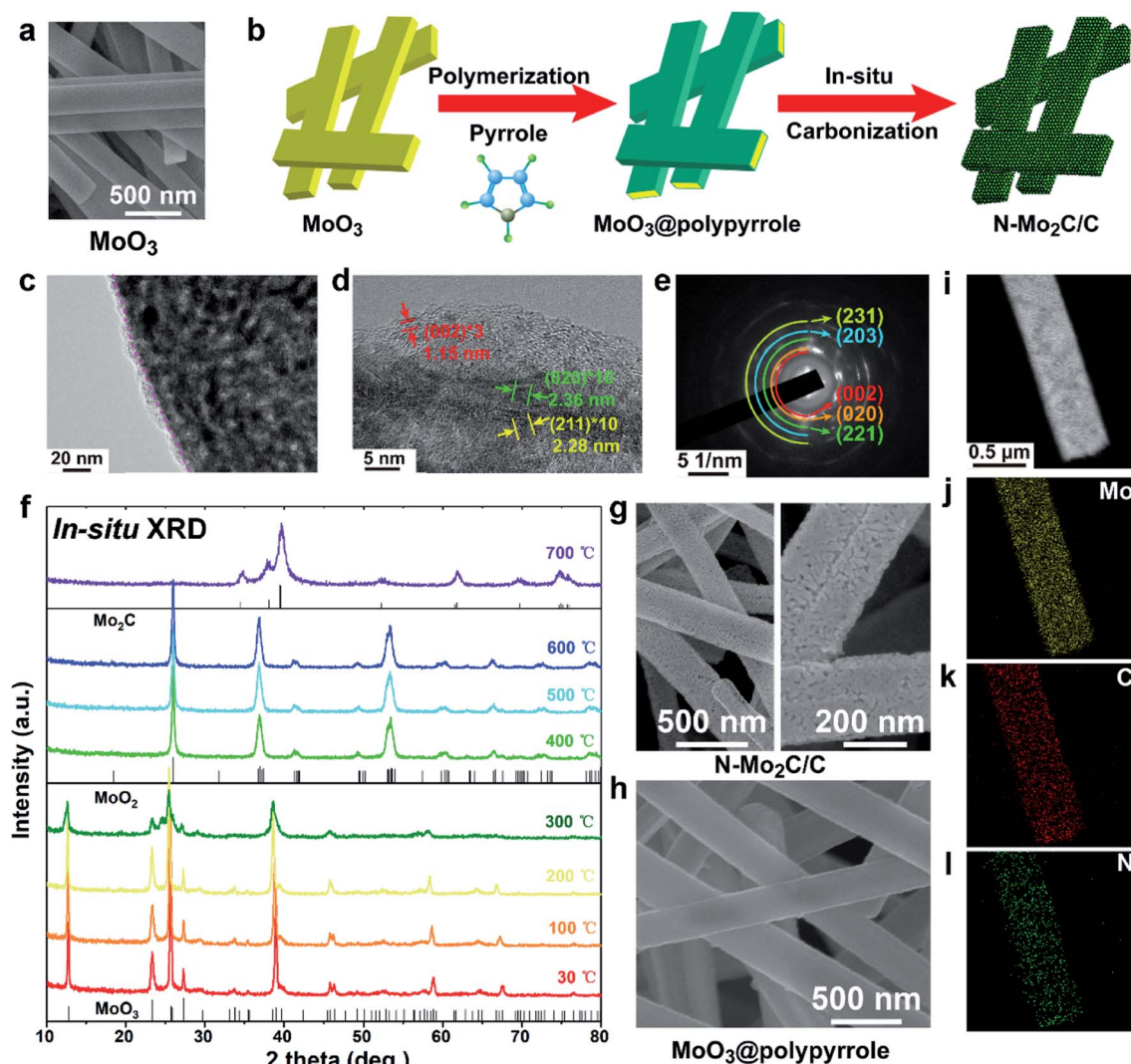

Fig. 1   (a) SEM image of the MoO$_3$; (b) schematic illustration for the formation process of the N-doped Mo$_2$C/C nanobelts; (c) TEM, (d) HRTEM and (e) SAED images of the N-Mo$_2$C/C nanobelts; (f) *in situ* XRD patterns, reflecting the phase change of the MoO$_3$@ppy powder along calcinations from 30 to 700 °C in a flowing nitrogen atmosphere; SEM images of (g) N-Mo$_2$C/C and (h) MoO$_3$@ppy; (i–l) STEM image and the corresponding Mo, C, and N elemental maps of N-Mo$_2$C/C.

This journal is © The Royal Society of Chemistry 2020

J. Mater. Chem. A, 2020, **8**, 7819–7827 | **7821**

200–300 nm and a relatively smooth surface, as shown in Fig. 1a. The following polymerization of PPY on the surface (MoO$_3$@ppy) does not change the morphology of the nanobelts (Fig. 1h). After subsequent calcination for the preparation of Mo$_2$C, the nanobelt structure is well kept and abundant nanoparticles were formed on the surface (Fig. 1g). A brief schematic of the formation procedure is accordingly shown in Fig. 1b.

The structure of Mo$_2$C is further investigated using TEM and the results are shown in Fig. 1c. It is found that the whole nanobelt is composed of small particles with a thin and uneven coating layer. Not only the surface but also the bulk of the nanobelt is porous. In an enlarged HRTEM view of Fig. 1d, apparent lattice fringe spacings of 0.228 and 0.236 nm that come from different crystal particles and correspond to the (211) and (020) planes of Mo$_2$C, respectively, are observed, confirming the phase composition of the nanoparticles. The surface coating layer with a thickness of several nanometers is defined to be C with a relatively large lattice space of 0.383 nm that is indexed to the typical (002) plane, implying the successful coating of C on the surface. Mass proportion of the C in the Mo$_2$C/C composite is around 9 wt% based on the TGA results (Fig. S1†). From the selected area electron diffraction (SAED) pattern (Fig. 1e), bright diffraction rings can be observed, which are attributed to the (002), (020), (221), (203) and (231) planes of Mo$_2$C, indicating a polycrystalline structure. Elemental mapping images (Fig. 1j–l) of one nanobelt (Fig. 1i) demonstrate that there are not only Mo and C elements but also evident N, indicating the doping of N. According to the above analysis, it can be concluded that during the pyrolysis process, N-Mo$_2$C/C is formed through carbonization and reduction accompanied by N doping, where PPY works as the N source for

doping and the C source for the carbonization of MoO$_3$ to form Mo$_2$C and excess C is left on the surface as coating layers.

Phase compositions and structural information of the final product were further determined using the XRD patterns and Raman spectra in Fig. 2 and b. XRD patterns of the white precipitate (blue curve of Fig. 2a) collected from the hydrothermal product match well with those of the orthorhombic MoO$_3$ phase (JCPDS no. 89-5108), confirming the formation of high purity and well-crystallized MoO$_3$. After pyrolysis, diffraction peaks located at 34.64, 38.02, 39.67, 52.23, 61.66, 69.58, and 74.83° in the red curve of Fig. 2a can be, respectively, ascribed to the (002), (020), (211), (221), (203), (231), and (223) planes of orthorhombic Mo$_2$C with a space group of $Pca2_1$ (JCPDS no. 77-0720). There are no other additional peaks, indicating the full conversion of MoO$_3$ to Mo$_2$C. The Raman spectra were also recorded for MoO$_3$ and N-Mo$_2$C/C and are shown in Fig. 2b. All the detectable Raman bands centered at 995, 818, 666, 378, 338, 291, 245, 159 and 128 cm^{-1} can be indexed to the orthorhombic MoO$_3$ (the blue curve). Characteristic D and G bands assigned to carbon can be detected and no Raman active vibrations indexed to Mo$_2$C can be observed for N-Mo$_2$C/C, which is in agreement with the other Mo$_2$C concerned reports.[26–28]

To gain detailed information on the N-doping, surface chemical composition of N-Mo$_2$C/C was further explored by XPS and fitted with the Gaussian law in Fig. 2d–f. Five peaks centered at around 232.08 eV, 284.08 eV, 398.08 eV, 416.08 eV and 530.08 eV that can be ascribed to Mo 3d, C 1s, N 1s, Mo 3p and O 1s, respectively, are distinguished from the survey spectrum (Fig. S2†). The high-resolution Mo 3d XPS spectrum (Fig. 2d) can be divided into six peaks, ascribable to Mo^{2+} (228.7 and 232.1 eV), Mo^{4+} (229.5 and 232.8 eV) and Mo^{6+} (232.6 and
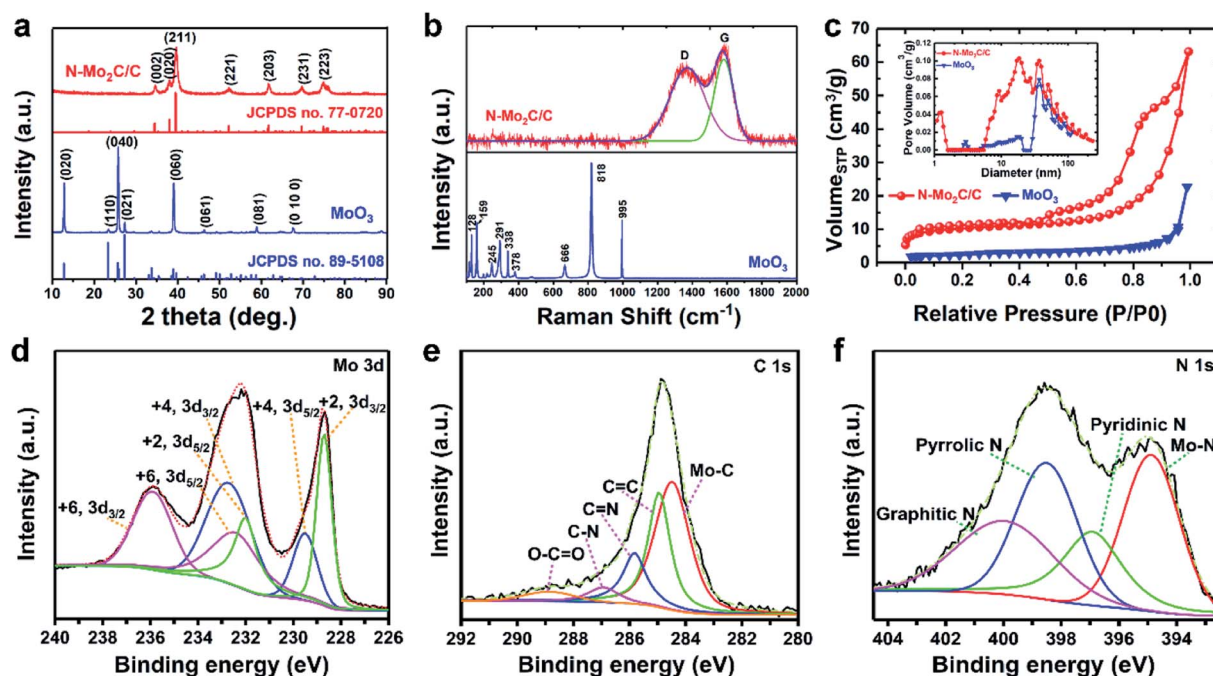

Fig. 2 (a) XRD patterns, (b) Raman spectra and (c) N$_2$ adsorption and desorption isotherms, the inset is pore size distributions of MoO$_3$ (blue) and N-Mo$_2$C/C (red); XPS spectra of (d) Mo 3d, (e) C 1s and (f) N 1s of N-Mo$_2$C/C.

7822 | *J. Mater. Chem. A*, 2020, **8**, 7819–7827

This journal is © The Royal Society of Chemistry 2020

235.9 eV) species,[29–31] respectively, implying partial surface oxidation of Mo_2C.[14,30,31] In the high-resolution C 1s spectrum (Fig. 2e), a characteristic peak of the Mo–C bond in Mo_2C at 284.5 eV, and four more peaks at 285.0 eV, 285.8 eV, 287.0 eV and 288.9 eV that correspond to C sp^2–C sp^2, N–C sp^2, N–C sp^3 and O–C≡O bonds, respectively, can be fitted, indicating that some of the N are successfully doped into the C matrix,[30,32] which is helpful for the electron transport. The high-resolution N 1s spectrum (Fig. 2f) was deconvoluted into four peaks: the peaks at 396.98, 398.7 and 400.1 eV can be assigned to pyridinic-N, pyrrolic-N and graphitic-N, respectively; the peak at 394.9 eV corresponds to the Mo–N bond,[23,30,32–34] indicating that there is also N-doping in the Mo_2C matrix. The Mo–N bond formed between the Mo_2C and the C coating layer is expected to maintain their well contact during reiterative charging/discharging, which is beneficial to the stability.[30,32,35]

Moreover, specific surface areas of MoO_3 and N-Mo_2C/C (Fig. 2c) are calculated to be 7.95 and 36.34 m^2 g^{-1}, respectively, using N_2 sorption and desorption isotherms with the Brunauer–Emmett–Teller (BET) theory. The higher specific surface area of the N-Mo_2C/C nanobelts than that of the MoO_3 nanobelts reflects that extra pores are formed during the carbonization process, which is in agreement with the SEM results. Detailed pore size distributions of MoO_3 (blue) and the N-Mo_2C/C (red) are shown in Fig. 2c. There are more pores for N-Mo_2C/C, which will facilitate the ion diffusion and will ease volume expansion during charging/discharging.

To evaluate the charge storage ability of the porous N-Mo_2C/C, CV and GCD measurements in a potential window of 0.01 to 3.0 V vs. Li/Li$^+$ were performed and the results are shown in Fig. 3. In the CV curves (Fig. 3a and b), a very weak redox pair with a cathodic peak at around 1.2 V and an anodic peak at about 1.5 V can be observed, and is ignorable when the sweep rates are higher than 20 mV s^{-1}. The redox pair has been attributed to the conversion reaction of $Mo_2C + xLi^+ + xe^- \rightarrow 2Mo^0 + Li_xC$ in the previous reports,[12,23,36] but no evidence that supports this view has ever been provided. More studies need to be carried out to disclose the origin of this redox pair.
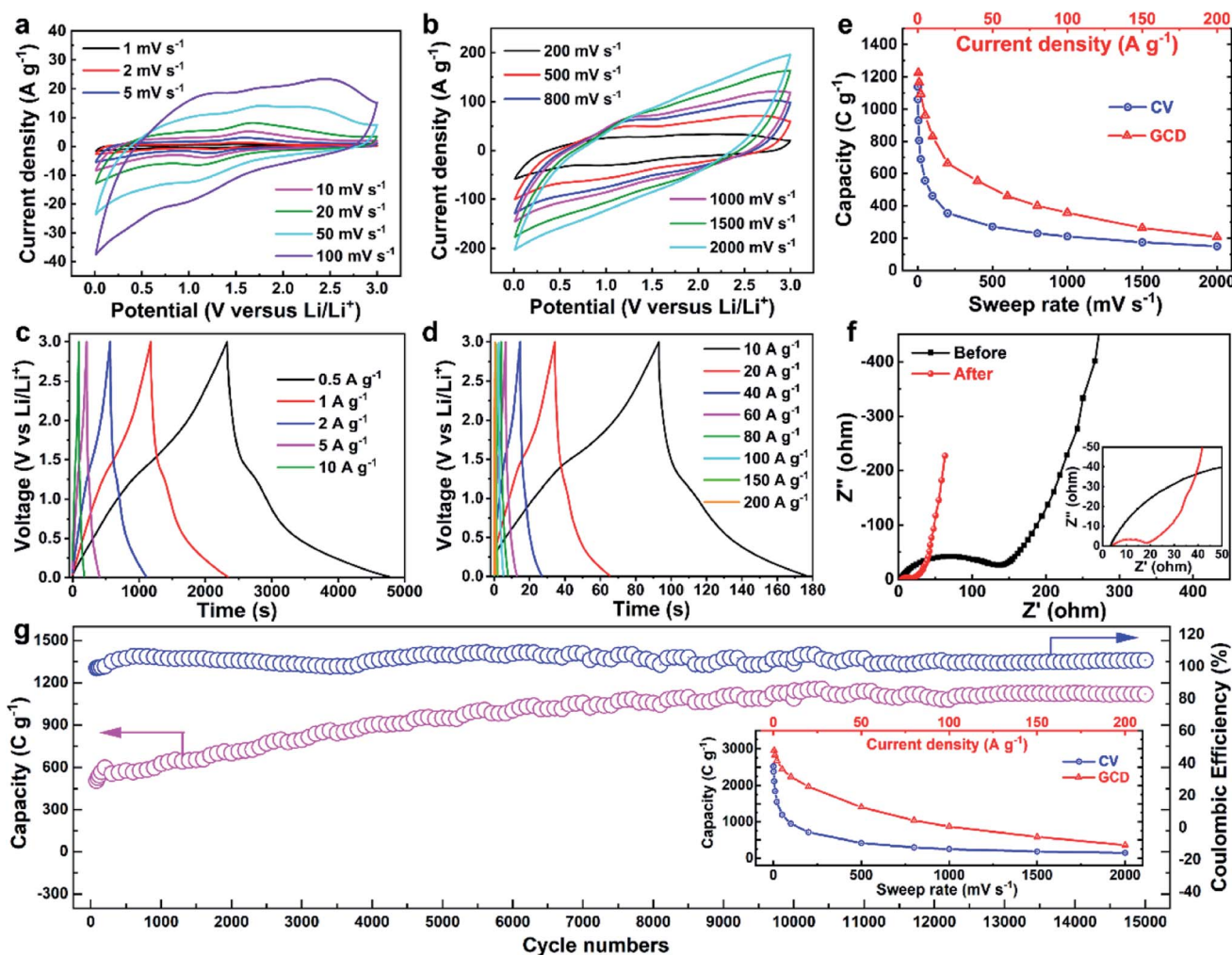

Fig. 3 Electrochemical performance of the N-Mo_2C/C nanobelts: (a) and (b) CV curves obtained at different scan rates from 1 to 2000 mV s^{-1} with a potential window ranging from 0.01 to 3 V (vs. Li/Li$^+$); (c) and (d) GCD curves tested at different current densities from 0.5 to 200 A g^{-1}; (e) gravimetric capacity plots calculated based on the CV (blue curve) and the GCD (red curve) results; (f) Nyquist plots before and after long-term cycling; (g) long-term cycling behavior measured at 50 mV s^{-1}, inset is the gravimetric capacity plots after cycling.

Consistently, negligible charge and discharge platforms at around 1.5 V/1.2 are observed in the near-linear GCD curves at different current densities from 0.5 to 200 A g^{-1} in Fig. 3c and d. Specific capacities calculated from the CV and the GCD results are shown in Fig. 3e. A capacity of 1139 C g^{-1} (316 mA h g^{-1}) can be achieved at a scan rate of 1 mV s^{-1} and still up to 151 C g^{-1} can be achieved at an extremely high scan rate of 2000 mV s^{-1}, which means considerable energy can be stored in less than 2 second. However, the capacity is up to 1225 C g^{-1} at a current density of 0.5 A g^{-1} and a high capacity of 208 C g^{-1} is maintained at 200 A g^{-1}, indicating high capability and remarkable rate performance, much better than those of most Mo-based electrochemical electrodes (Table S1†), especially in organic electrolytes.[37–39]

In addition, long-term cycling stability, another important parameter to evaluate the N-Mo$_2$C/C electrode, is characterized at 50 mV s^{-1} in Fig. 3g. Surprisingly, there is no decay but an obvious increase in the capacity upon cycling, gradually increasing in the first 5000 cycles and then maintained in the following 10, 000 cycles with a final capacity as high as ~1120 C g^{-1}. There is another thing worth mentioning that the coulombic efficiency is close to 100% during the whole cycling test (blue curve in Fig. 3g). After cycling, the capacity can reach 2523 C g^{-1} at 1 mV s^{-1} and 2950 C g^{-1} at 0.5 A g^{-1}, and still be capable of up to 358 C g^{-1} at 200 A g^{-1} (see Fig. S3† and the inset of Fig. 3g). The performance enhancement should be concerned with the impedance decline after cycling, as shown in the EIS of Fig. 3f.

To conduct more in-depth investigations, the morphological and structural changes of the electrode after cycling were also studied with SEM (Fig. S4†) and HRTEM (Fig. S5†). From the

SEM image, it can be seen that the nanobelt structure is well maintained with a more porous surface (see the zoom-in image of Fig. S4b†). From the HRTEM images (Fig. S5b†), no obvious crystal particles or lattice fringes can be observed, implying that the well patterned crystal structure is destroyed and an amorphous structure is formed after long-term cycling, which is consistent with the SAED patterns (Fig. S5c†), no spots or circular arcs can be observed. Moreover, the shell seems to be thicker, close to ~20 nm after cycling (see Fig. S5a†), which is only several nanometers before cycling (see Fig. 1c). Therefore, there are three possible reasons for the capacity enhancement: the better wetting property of the electrolyte owing to the more porous structure of the electrode, the improved diffusion and accommodation ability of electrolyte ions because of the disappearance of grain boundaries at the interface and the bulk (activity process of the material itself) and the possible formation of an organic polymeric layer resulting from the decomposition of the electrolyte, which can deliver excess capacity.[40–44]

In order to gain insight into the charge storage mechanism, the dependence of peak current (i) on the sweep rate (v) is evaluated in Fig. 4. The plot of $\log(i)$ *versus* $\log(v)$ from 0.1 to 10 mV s^{-1} is displayed in Fig. 4a and the b value that reflects the contribution of the capacitive process is calculated with the power law: $i = av^b$, where a and b are alterable parameters.[19,37,45] It is well accepted that the current response is a diffusion-controlled battery-type process when $b = 0.5$ while it is a surface-controlled capacitive process when $b = 1$.[46] For the N-Mo$_2$C/C electrode, high b values of 0.91 and 0.9 are obtained for the cathodic and anodic peaks, respectively, implying that the surface capacitive effect is predominant. In detail, it is a combination of two mechanisms, the surface-controlled
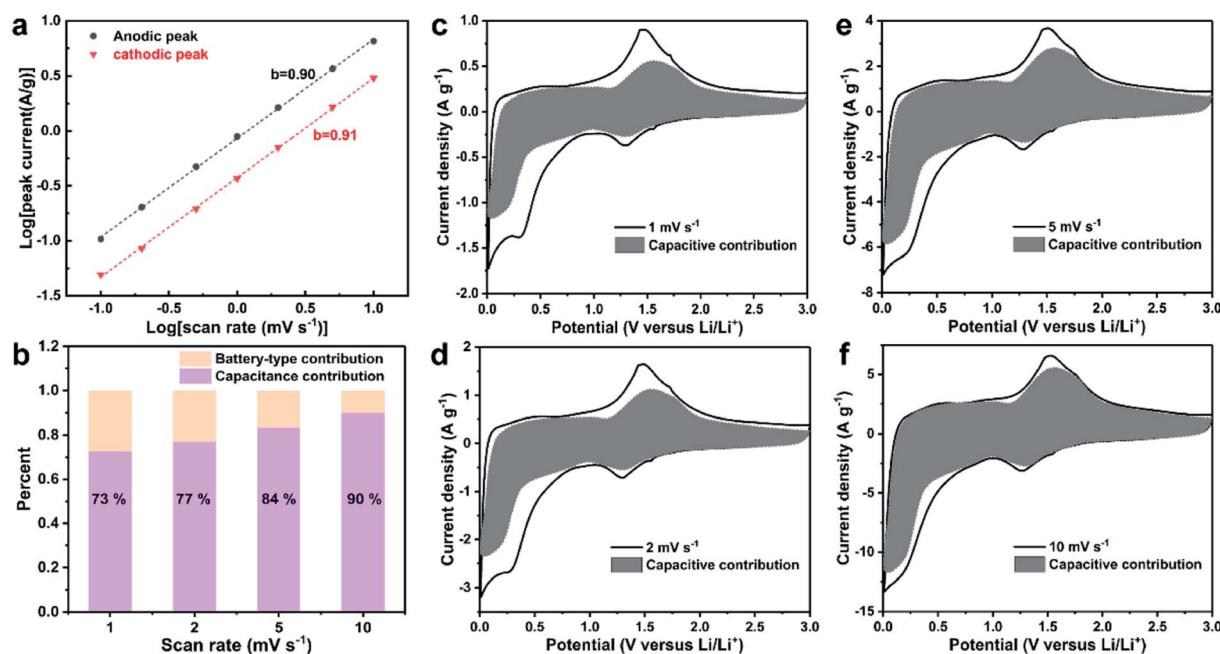

Fig. 4 (a) Plots of anodic (black curve) and cathodic (red curve) peak current against the scan rate from 0.1 to 10 mV s^{-1} for N-Mo$_2$C/C, slopes of these lines reflect b values; (b) surface-controlled capacitive contribution to the capacity at different scan rates; capacitive contribution represented by gray areas at different scan rates of (c) 1 mV s^{-1}, (d) 2 mV s^{-1}, (e) 5 mV s^{-1} and (f) 10 mV s^{-1}.

7824 | J. Mater. Chem. A, 2020, 8, 7819–7827

This journal is © The Royal Society of Chemistry 2020

capacitive mechanism (k_1v) and the diffusion-controlled mechanism ($k_2v^{1/2}$), expressed as: $i(V) = k_1v + k_2v^{1/2}$, where k_1 and k_2 are alterable parameters.[46] By determining the values of k_1 and k_2, the fraction of the current caused by capacitive contribution and battery-type contribution can be determined.

As shown in Fig. 4c–f, the gray areas represent the capacitive contribution at 1, 2, 5, and 10 mV s^{-1}. The ratio of capacitive contribution increases along with the sweep rate up to 90% at 10 mV s^{-1}, as shown in Fig. 4b. Even when the sweep rate is low as 1 mV s^{-1}, the capacitive contribution is still up to ~73%, indicating that the charge storage process is predominantly surface limited and the charge diffusion in the bulk is very fast, which should be the main reason for the high rate performance.

Structure evolution of the N-Mo$_2$C/C electrode during charging/discharging is investigated by *in situ* SXRD measurement in Fig. 5 and S6.† During this measurement, the half-cell was firstly discharged to 0.01 V from an open circuit potential (OCP) of around 2.6 V and then charged to 3 V. The result shows that no new Bragg peaks are seen except those indexed to Mo$_2$C. The peaks of Mo$_2$C remain almost intact during one charging/discharging cycle, and gradually weaken during long-term

cycling. From the partially enlarged patterns in Fig. S6,† slight shifts of the (002), (211), and (203) peaks to a lower angle during discharging can be observed, indicating a very slight expansion of the Mo$_2$C crystals. Opposite changes can be observed during charging. The size of the zigzag 1D tunnel along the z-axis is rather large, as shown in Fig. 5a, the slight change of the crystal structure of Mo$_2$C implies that most of the charge is stored in the tunnels through fast diffusion and insertion-type capacity makes the main contribution, which agrees well with the above analysis shown in Fig. 4.

The initial capacitance of the N-Mo$_2$C/C electrode is higher than the theoretical value evaluated from the one electron concerned insertion mechanism. After activation of long-term cycling, the capacitance is increased and is even higher than the theoretical value (1892 C g^{-1}/524 mA h g^{-1}) calculated according to the well-accepted phase conversion mechanism (Mo$_2$C to Mo). While no LiC$_6$ or Mo phases is identified in the synchrotron XRD pattern even at the fully discharged state (0.1 V). Massive formation of their amorphous phases can also be excluded by the negligible intensity change of the Mo$_2$C peaks in a whole charging/discharging cycle (see Fig. 5b). It can be
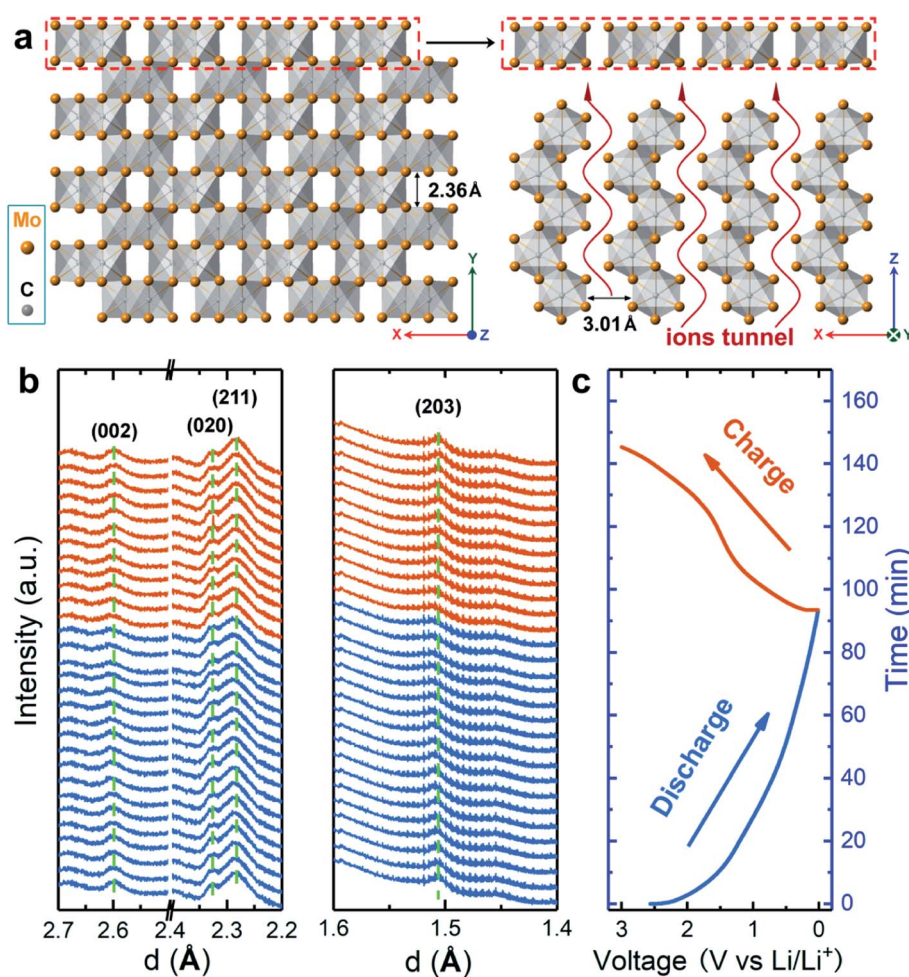

Fig. 5 (a) Typical crystal structure of the Mo$_2$C viewed from different directions; (b) *in situ* SXRD patterns of the N–Mo$_2$C/C electrode in selected d-spacing ranges, highlighting the evolution of the (002), (020), (211) and (203) peaks of Mo$_2$C; (c) charging/discharging curve collected during the *in situ* test.

This journal is © The Royal Society of Chemistry 2020

J. Mater. Chem. A, 2020, **8**, 7819–7827 | **7825**

concluded that most of the charges are stored in the 1D tunnel, while the detailed occupying mode needs further investigation.

4. Conclusion

In this work, a co-step of doping and carbonization is developed to fabricate structurally stable N-doped Mo_2C/C for ultrafast and high-energy storage. Benefiting from the natural properties of Mo_2C (good electronic conductivity and natural tunnel structure suited for fast ionic diffusion) and the well-designed structure of the composite, the electrodes exhibit fast and high energy storage ability. High initial capacitances of 1139 C g^{-1} at 1 mV s^{-1}, 151 C g^{-1} at an extremely high scan rate of 2000 mV s^{-1} and 208 C g^{-1} at 200 A g^{-1} are achieved. After long-term cycling for 15 000 cycles, the capacitances are improved to be 2523 C g^{-1} at 0.5 A g^{-1} and 1403 C g^{-1} at 50 A g^{-1}. The charge storage mechanism of the electrode is evaluated with the power law and *in situ* synchrotron XRD measurements. It is found that a surface-controlled capacitive process makes the main contribution to the capacity, over 90% when the sweep rate is higher than 10 mV s^{-1} and still high as 73% at 1 mV s^{-1}. There is no phase change but very slight and reversible crystal expansion/contraction during discharging/charging, implying that most of the charges are stored in the 1D tunnels, a typical feature of the insertion-type pseudocapacitive electrode. The good electrochemical performance of the Mo_2C/C composite makes it a promising candidate to achieve high power and energy density simultaneously.

Conflicts of interest

There are no conflicts to declare.

Acknowledgements

References

1 M. Winter and R. J. Brodd, *Chem. Rev.*, 2004, **104**, 4245–4269.

2 J. R. Miller and P. Simon, *Science*, 2008, **321**, 651–652.

3 L. Yuting, H. Rong, F. Yongzheng, Z. Kai, C. Kui, Y. Jun, Y. Ke, W. Guiling and C. Dianxue, *Nano-Micro Lett.*, 2019, **11**, 30.

4 P. Simon and Y. Gogotsi, *Nat. Mater.*, 2008, **7**, 845–854.

5 P. Zhibin, H. Haibo, L. Guojin and Y. Changhui, *Nano-Micro Lett.*, 2017, **9**, 19.

6 L. L. Zhang and X. S. Zhao, *Chem. Soc. Rev.*, 2009, **38**, 2520–2531.

7 J. Li, X. Yun, Z. Hu, L. Xi, N. Li, H. Tang, P. Lu and Y. Zhu, *J. Mater. Chem. A*, 2019, **7**, 26311–26325.

8 G. Wang, L. Zhang and J. Zhang, *Chem. Soc. Rev.*, 2012, **41**, 797–828.

9 H. H. Hwu and J. G. Chen, *Chem. Rev.*, 2005, **105**, 185–212.

10 J. A. Nelson and M. J. Wagner, *Chem. Mater.*, 2002, **14**, 1639–1642.

11 X.-R. Shi, J. Wang and K. Hermann, *J. Phys. Chem. C*, 2010, **114**, 13630–13641.

12 Y. Xiao, L. Zheng and M. Cao, *Nano Energy*, 2015, **12**, 152–160.

13 Q. Sun, Y. Dai, Y. Ma, T. Jing, W. Wei and B. Huang, *J. Phys. Chem. Lett.*, 2016, **7**, 937–943.

14 C. Wan, Y. N. Regmi and B. M. Leonard, *Angew. Chem., Int. Ed.*, 2014, **53**, 6407–6410.

15 S. B. Yin, M. Cai, C. X. Wang and P. K. Shen, *Energy Environ. Sci.*, 2011, **4**, 558–563.

16 Z. X. Yan, H. E. Wang, M. P. Zhang, Z. F. Jiang, T. S. Jiang and J. M. Xie, *Electrochim. Acta*, 2013, **95**, 218–224.

17 M. Naguib, J. Come, B. Dyatkin, V. Presser, P. L. Taberna, P. Simon, M. W. Barsoum and Y. Gogotsi, *Electrochem. Commun.*, 2012, **16**, 61–64.

18 Z. F. Lin, D. Barbara, P. L. Taberna, K. L. Van Aken, B. Anasori, Y. Gogotsi and P. Simon, *J. Power Sources*, 2016, **326**, 575–579.

19 J. Yan, C. E. Ren, K. Maleski, C. B. Hatter, B. Anasori, P. Urbankowski, A. Sarycheva and Y. Gogotsi, *Adv. Funct. Mater.*, 2017, **27**, 1701264.

20 O. Mashtalir, M. R. Lukatskaya, M. Q. Zhao, M. W. Barsoum and Y. Gogotsi, *Adv. Mater.*, 2015, **27**, 3501–3506.

21 M. Naguib, J. Halim, J. Lu, K. M. Cook, L. Hultman, Y. Gogotsi and M. W. Barsoum, *J. Am. Chem. Soc.*, 2013, **135**, 15966–15969.

22 Z. Xu, X. Lv, J. Chen, L. Jiang, Y. Lai and J. Li, *Phys. Chem. Chem. Phys.*, 2017, **19**, 7807–7819.

23 Q. Gao, X. Zhao, Y. Xiao, D. Zhao and M. Cao, *Nanoscale*, 2014, **6**, 6151–6157.

24 W. Tian, H. Hu, Y. Wang, P. Li, J. Liu, J. Liu, X. Wang, X. Xu, Z. Li, Q. Zhao, H. Ning, W. Wu and M. Wu, *ACS Nano*, 2018, **12**, 1990–2000.

25 S. H. Liu, F. Li, D. Wang, C. M. Huang, Y. M. Zhao, J. B. Baek and J. X. Xu, *Small Methods*, 2018, **2**, 1800040.

26 M. Li, Y. Zhu, H. Wang, C. Wang, N. Pinna and X. Lu, *Adv. Energy Mater.*, 2019, **9**, 1803185.

27 D. Hou, J. Zhang, Q. Li, P. Zhang, C. Chen, D. Yan and Y. Mai, *Langmuir*, 2018, **34**, 10924–10931.

28 J. Zhu, Y. Yao, Z. Chen, A. Zhang, M. Zhou, J. Guo, W. D. Wu, X. D. Chen, Y. Li and Z. Wu, *ACS Appl. Mater. Interfaces*, 2018, **10**, 18761–18770.

29 Y. Zhao, K. Kamiya, K. Hashimoto and S. Nakanishi, *J. Am. Chem. Soc.*, 2015, **137**, 110–113.

30 R. Ma, Y. Zhou, Y. Chen, P. Li, Q. Liu and J. Wang, *Angew. Chem., Int. Ed.*, 2015, **54**, 14723–14727.

31 H. Lin, Z. Shi, S. He, X. Yu, S. Wang, Q. Gao and Y. Tang, *Chem. Sci.*, 2016, **7**, 3399–3405.

7826 | *J. Mater. Chem. A*, 2020, **8**, 7819–7827

This journal is © The Royal Society of Chemistry 2020

32 Y. Lu, H. Ang, Q. Yan and E. Fong, *Chem. Mater.*, 2016, **28**, 5743–5752.

33 J. T. Ren, L. Chen, C. C. Weng, G. G. Yuan and Z. Y. Yuan, *ACS Appl. Mater. Interfaces*, 2018, **10**, 33276–33286.

34 C. Lu, D. Tranca, J. Zhang, F. N. Rodri Guez Hernandez, Y. Su, X. Zhuang, F. Zhang, G. Seifert and X. Feng, *ACS Nano*, 2017, **11**, 3933–3942.

35 R. Li, S. Wang, W. Wang and M. Cao, *Phys. Chem. Chem. Phys.*, 2015, **17**, 24803–24809.

36 J. Zhu, K. Sakaushi, G. Clavel, M. Shalom, M. Antonietti and T. P. Fellinger, *J. Am. Chem. Soc.*, 2015, **137**, 5480–5485.

37 H. S. Kim, J. B. Cook, H. Lin, J. S. Ko, S. H. Tolbert, V. Ozolins and B. Dunn, *Nat. Mater.*, 2017, **16**, 454–460.

38 G. Zhang, T. Xiong, M. Yan, L. He, X. Liao, C. He, C. Yin, H. Zhang and L. Mai, *Nano Energy*, 2018, **49**, 555–563.

39 B. Yu, D. Yang, Y. Hu, J. He, Y. Chen and W. He, *Small Methods*, 2019, **3**, 1800287.

40 H. Wu, G. Yu, L. Pan, N. Liu, M. T. McDowell, Z. Bao and Y. Cui, *Nat. Commun.*, 2013, **4**, 1943.

41 Y. Sun, X. Hu, W. Luo, F. Xia and Y. Huang, *Adv. Funct. Mater.*, 2013, **23**, 2436–2444.

42 X. Wu, Z. Wang, M. Yu, L. Xiu and J. Qiu, *Adv. Mater.*, 2017, **29**, 1607017.

43 L. Wang, Q. Zhang, J. Zhu, X. Duan, Z. Xu, Y. Liu, H. Yang and B. Lu, *Energy Storage Mater.*, 2019, **16**, 37–45.

44 Q. Zhang, L. Wang, J. Wang, X. Yu, J. Ge, H. Zhang and B. Lu, *J. Mater. Chem. A*, 2018, **6**, 9411–9419.

45 H. Lindstrom, S. Sodergren, A. Solbrand, H. Rensmo, J. Hjelm, A. Hagfeldt and S. E. Lindquist, *J. Phys. Chem. B*, 1997, **101**, 7717–7722.

46 J. Wang, J. Polleux, J. Lim and B. Dunn, *J. Phys. Chem. C*, 2007, **111**, 14925–14931.